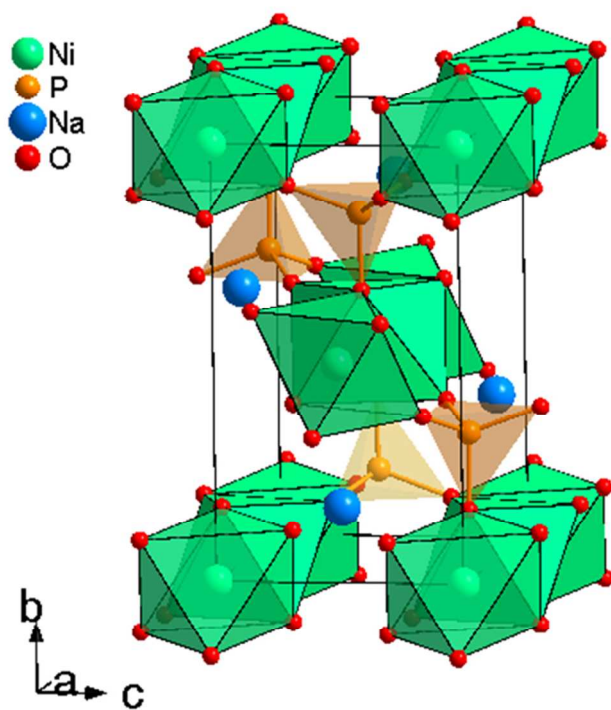




**Synthesis and Electrochemical Performances of Maricite-  
NaMPO<sub>4</sub> (M=Ni, Co, Mn) Electrodes for Hybrid  
Supercapacitors**

Journal:	<i>RSC Advances</i>
Manuscript ID:	RA-ART-06-2014-006050.R1
Article Type:	Paper
Date Submitted by the Author:	19-Sep-2014
Complete List of Authors:	Baskar, Senthilkumar; Bharathiar University, Physics; Vijaya Sankar, Kalimuthu; Bharathiar University, Physics Vasylechko, Leonid; Lviv Polytechnic National University, Semiconductor Electronics Lee, Yun-Sung; Chonnam National University, Applied Chemical Engineering Ramakrishnan, Kalai; Bharathiar University, Physics



254x190mm (96 x 96 DPI)

Cite this: DOI: 10.1039/c0xx00000x

www.rsc.org/xxxxxx

ARTICLE TYPE

# Synthesis and Electrochemical Performances of Maricite-NaMPO<sub>4</sub> (M=Ni, Co, Mn) Electrodes for Hybrid Supercapacitors

Baskar Senthilkumar<sup>a</sup>, Kalimuthu Vijaya Sankar<sup>a</sup>, Leonid Vasylechko<sup>b</sup>, Yun-Sung Lee<sup>c</sup> and Ramakrishnan Kalai Selvan<sup>\*a</sup>

Received (in XXX, XXX) Xth XXXXXXXXX 20XX, Accepted Xth XXXXXXXXX 20XX

DOI: 10.1039/b000000x

Sodium metal phosphates, NaMPO<sub>4</sub> (M = Mn, Co and Ni) were successfully synthesized by solution combustion synthesis (SCS) method using glycine-nitrate as a precursor. XRD Rietveld refinement method was revealed the crystal structure and lattice parameters of NaMPO<sub>4</sub> (M = Mn, Co and Ni). For the first time, the crystal structure parameters of the orthorhombic NaNiPO<sub>4</sub> maricite-type phase were evaluated. Similarly, it was identified that the NaCoPO<sub>4</sub> and NaMnPO<sub>4</sub> have high temperature hexagonal and maricite phase, respectively. The calculated BET specific surface area ( $S_{\text{BET}}$ ) of NaMnPO<sub>4</sub>, NaCoPO<sub>4</sub> and NaNiPO<sub>4</sub> were 17.7, 22.6 and 18.7 m<sup>2</sup> g<sup>-1</sup>, respectively. The NaMPO<sub>4</sub> (M = Mn, Co and Ni) electrode exhibits good specific capacitance in 1 M NaOH electrolyte, when compared with 1 M Na<sub>2</sub>SO<sub>4</sub>, 1 M NaNO<sub>3</sub> and 1 M NaCl. This difference in specific capacitance was analysed based on the influence of electrolyte anions (Cl<sup>-</sup>, SO<sub>4</sub><sup>2-</sup>, OH<sup>-</sup> and NO<sub>3</sub><sup>-</sup>) and pH conditions of the electrolyte solution. Overall, maricite-NaNiPO<sub>4</sub> nanoparticles provided a high specific capacitance of 368 F g<sup>-1</sup> compared to NaMnPO<sub>4</sub> (163 F g<sup>-1</sup>) and NaCoPO<sub>4</sub> (249 F g<sup>-1</sup>) in 1 M NaOH electrolyte. Subsequently, hybrid supercapacitor (AC||NaNiPO<sub>4</sub>) was fabricated and it delivered a good specific capacitance and cyclic stability than the commercially available device.

## 1. Introduction

Among various energy storage devices, Li-ion batteries are promising power sources for cell phones, laptops, digital cameras, power tools and electric vehicles owing to its high energy density.<sup>1,2</sup> However its broad applications in grid storage are limited due to the high cost, low abundance of Li metal and organic electrolytes.<sup>3</sup> Next to Li, Na is second metallic element having lower ionic radius (0.97 Å) and similar intercalating properties of Li. Therefore in order to decrease the cost and improve the safety, using both Na- based intercalating materials and aqueous electrolyte used is one of the recent strategies instead of Li based materials.<sup>3,4</sup> In this regard, various sodium based electrode materials including NaFePO<sub>4</sub>,<sup>5</sup> Na<sub>4</sub>Mn<sub>9</sub>O<sub>18</sub>,<sup>6</sup> Na<sub>x</sub>MnO<sub>2</sub>,<sup>7</sup> NaVPO<sub>4</sub>F,<sup>8</sup> NaCrO<sub>2</sub>,<sup>9</sup> NaNi<sub>1/3</sub>Co<sub>1/3</sub>Mn<sub>1/3</sub>PO<sub>4</sub>,<sup>10</sup> Na[Ni<sub>1/3</sub>Co<sub>1/3</sub>Mn<sub>1/3</sub>]O<sub>2</sub><sup>11</sup> and Na<sub>4</sub>Co<sub>3</sub>(PO<sub>4</sub>)<sub>2</sub>P<sub>2</sub>O<sub>7</sub><sup>12</sup> have been experienced as electrode materials for energy storage applications due to its Na-ion intercalating properties, low cost and environmental friendliness.<sup>5-12</sup> Initially, layered sodium manganese oxide (NaMnO<sub>2</sub>) has been proposed as cathode materials for Na-ion batteries.<sup>7</sup> Among the Na based cathodes, NaMnO<sub>2</sub> delivered high specific capacity of 140 mAh g<sup>-1</sup> due to its six biphasic transitions.<sup>13</sup> However, these materials delivered poor cycling performance since its multiple phase transition Na insertion/de-insertion reactions.<sup>7,14</sup>

As well as sodium metal phosphates having the general chemical formula of NaMPO<sub>4</sub> (M=Mn, Co and Fe) have also been studied as electrode materials for sodium ion batteries.<sup>5,15-17</sup> Thermal stability and higher voltage due to the inductive effect

are the reasons for phosphate based materials to be the promising cathode materials in Na-ion batteries.<sup>18,19</sup> Recently, NaFePO<sub>4</sub>/C was prepared by potentiodynamic polarization in saturated aqueous NaNO<sub>3</sub> solution, which delivered a high storage capacity of 118 mAh g<sup>-1</sup> compared to LiFePO<sub>4</sub>/C.<sup>20</sup> Normally NaMPO<sub>4</sub> (M=Mn, Co and Fe) exhibits thermodynamically stable maricite structure, where transition metal ions occupies M(1) site, and sodium occupied M(2) sites, which is completely reversed in olivine structure. It was believed that the maricite structure is electrochemically inactive as a cathode material for battery applications in non aqueous media.<sup>21</sup> On the other hand, recent works demonstrated that the maricite structure is actively involved in charge storage process in alkali aqueous (NaOH) electrolyte.<sup>10,15</sup> However, to the best of our knowledge, there is no report available on the supercapacitive performance of pristine NaMPO<sub>4</sub> (M=Mn, Co and Ni).

In this present work, we have demonstrated that the synthesis of sodium metal phosphates (NaMPO<sub>4</sub>; M= Mn, Co and Ni) by solution combustion method using glycine-nitrate as precursors. The presence of nano-pores on the surface of the particles was clearly observed from field emission scanning electron microscope image (FE-SEM). The intercalation/de-intercalation properties of Na ion in maricite-type structured NaMnPO<sub>4</sub> were investigated. The orthorhombic maricite-NaNiPO<sub>4</sub> nanoparticles provided higher capacitance of 368 F g<sup>-1</sup> compared to hexagonal high temperature phase-NaCoPO<sub>4</sub> (249 F g<sup>-1</sup>) and maricite-NaMnPO<sub>4</sub> (195 F g<sup>-1</sup>) in 1 M NaOH electrolyte. A hybrid supercapacitor is fabricated using NaNiPO<sub>4</sub> and activated carbon (AC) as positive and negative electrodes, respectively. The hybrid

supercapacitor delivered excellent electrochemical performances relative to the commercially available device (AC||AC).

## 2. Experimental section

### 2.1 Materials

Sodium nitrate ( $\text{NaNO}_3$ ), manganese nitrate tetrahydrate ( $\text{Mn}(\text{NO}_3)_2 \cdot 4\text{H}_2\text{O}$ ), cobalt nitrate hexahydrate ( $\text{Co}(\text{NO}_3)_2 \cdot 6\text{H}_2\text{O}$ ), nickel nitrate hexahydrate ( $\text{Ni}(\text{NO}_3)_2 \cdot 6\text{H}_2\text{O}$ ), ammonium dihydrogen phosphate ( $\text{NH}_4\text{H}_2\text{PO}_4$ ), glycine ( $\text{C}_2\text{H}_5\text{NO}_2$ ), sodium hydroxide ( $\text{NaOH}$ ) and aqueous ammonia ( $\text{NH}_3 \cdot \text{H}_2\text{O}$ ) were purchased from Merck and used as received without further purification.

### 2.2 Synthesis of $\text{NaMPO}_4$ , (M=Mn, Co and Ni)

For the synthesis of maricite  $\text{NaMnPO}_4$ , a stoichiometric amount of  $\text{Mn}(\text{NO}_3)_2 \cdot 4\text{H}_2\text{O}$  (2.073 g),  $\text{NaNO}_3$  (0.8499 g) and  $\text{NH}_4\text{H}_2\text{PO}_4$  (1.150 g) were dissolved in desired amount of distilled water and mixed with the above solutions. The desired amount of glycine was dissolved in distilled water and poured into above solution. In this reaction, oxidant to fuel ratio was maintained as 1. Further, the pH of the precursor solution was adjusted to 7 by adding ammonia solution. The resulting solution was placed on hot plate at  $200^\circ\text{C}$  for dehydration. After complete dehydration, the remaining solid mass was transferred into muffle furnace and the temperature was raised to  $300^\circ\text{C}$ . After 10 minutes, decomposition occurred with gradual release of gaseous by-products. The final foamy product was collected after grinding it on agate mortar pestle and then used for further characterization. The foamy product was calcined at  $400^\circ\text{C}$  for 3h to form the single phase  $\text{NaMnPO}_4$ . The similar procedure was repeated for the synthesis of  $\text{NaCoPO}_4$  and  $\text{NaNiPO}_4$  by using  $\text{Co}(\text{NO}_3)_2 \cdot 6\text{H}_2\text{O}$  and  $\text{Ni}(\text{NO}_3)_2 \cdot 6\text{H}_2\text{O}$ , respectively. Here, the single phase of  $\text{NaNiPO}_4$  was obtained after  $700^\circ\text{C}$  calcinations and  $\text{NaCoPO}_4$  phase was obtained without any calcinations.

### 2.3 Characterization techniques

Phase formation was identified by powder X-ray diffractometer (Bruker, D8 advance) with  $\text{CuK}\alpha$  radiation. A quantitative two-phase full-profile Rietveld refinement has been performed by using WinCSD program package. To investigate the morphology of the prepared samples, JEOL JEM 2100 High Resolution Transmission Electron Microscope (HRTEM) with 200 kV acceleration voltages was used. The surface area and pore size distribution of the composites were investigated by  $\text{N}_2$  adsorption-desorption experiments at 77 K using Micromeritics ASAP 2010 surface area analyser. The electrochemical performances of  $\text{NaMPO}_4$ , (M=Mn, Co and Ni) were investigated using cyclic voltammetry (CV) and galvanostatic charge-discharge techniques. The electrochemical experiments were carried out in three electrode system using platinum wire as a counter electrode.  $\text{Ag}/\text{AgCl}$  and  $\text{Hg}/\text{HgO}$  were used as a reference electrode. Aqueous solution of 1 M  $\text{Na}_2\text{SO}_4$ , 1 M  $\text{NaCl}$ , 1 M  $\text{NaNO}_3$  and 1 M  $\text{NaOH}$  were used as electrolyte. The cyclic voltammetry and galvanostatic charge-discharge studies of the composites were carried out using SP-150, Bio-Logic Science Instruments in room temperature.

### 2.4 Electrode preparation

To prepare active electrode material,  $\text{NaMPO}_4$  (80 wt %), carbon black (15 wt %) and polyvinylidene fluoride (PVDF) (5 wt

%) were suspended in 0.4 mL of N-methyl-2-pyrrolidinone (NMP) to form a slurry. The slurry was coated on a small piece of graphite sheet (area of coating,  $1\text{ cm}^2$ ). The loaded active material was approximately 2 mg in each case. Activated carbon (AC) was purchased from Aldrich with surface area of  $\sim 1800\text{ m}^2\text{g}^{-1}$ . To prepare active negative electrode material, AC (90 wt %) and polyvinylidene fluoride (PVDF) (10 wt %) were used. A hybrid full cell ( $\text{AC}||\text{NaNiPO}_4$ ) was fabricated by employing a polypropylene separator.

## 3. Results and discussion

### 3.1 Structural analysis

XRD pattern of combustion synthesized sodium metal phosphates ( $\text{NaMPO}_4$ , M=Mn, Co and Ni) are shown in Fig. 1 (a-c). The observed diffraction maxima for  $\text{NaMnPO}_4$  (Fig. 1 (a)) is basically matched with the standard diffraction pattern of maricite-type phase (JCPDS no. 84-0852). Full profile Rietveld refinement confirms the phase composition of  $\text{NaMnPO}_4$  (see Fig. S1) and allows establishing the lattice parameters of the orthorhombic  $\text{NaMnPO}_4$ . Refined values of the cell dimensions of  $\text{NaMnPO}_4$  in comparison with the literature data for the reference compound are given in Table 1. The calculated lattice parameters are consistent with the reported values.

On the other hand, the majority of observed diffraction peaks of combustion synthesized  $\text{NaCoPO}_4$  (Fig. 1 (b)) are matched with the standard diffraction pattern of the high temperature  $\beta$ -phase of  $\text{NaCoPO}_4$  (JCPDS no. 52-0335), which belongs to the family of stuffed tridymites. As it is derived from the quantitative XRD phase analysis, performed by two-phase Rietveld refinement, the sample shows coexistence of two  $\text{NaCoPO}_4$  polymorphs - 77 wt. % of hexagonal  $\text{NaCoPO}_4$  phase and 23 wt. % of orthorhombic maricite-type  $\text{NaCoPO}_4$  phase (Fig.S2). Refined values of the cell dimensions of two  $\text{NaCoPO}_4$  polymorphs detected in the sample is given in Table 1, in comparison with the literature data for the reference compounds. Lattice parameters of combustion synthesized  $\text{NaCoPO}_4$  is well matched with reported high temperature hexagonal  $\text{NaCoPO}_4$ .

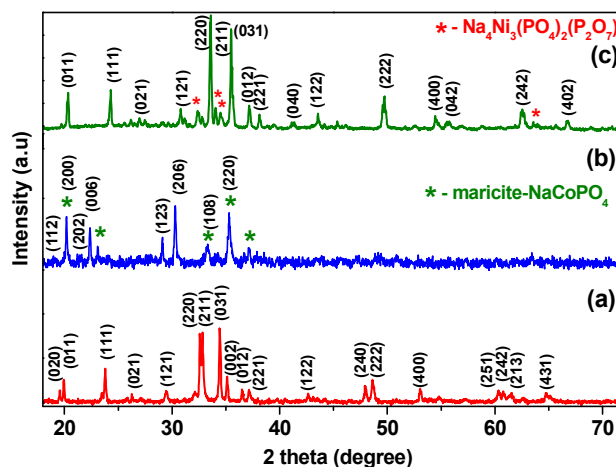
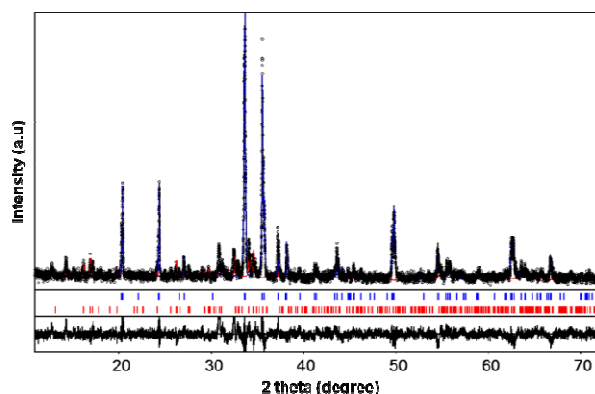


Fig. 1. XRD pattern of combustion synthesized (a)  $\text{NaMnPO}_4$ , (b)  $\text{NaCoPO}_4$  and (c)  $\text{NaNiPO}_4$ .

From the XRD pattern of  $\text{NaNiPO}_4$  (Fig. 1 (c)), orthorhombic maricite-type  $\text{NaNiPO}_4$  is detected as the main phase. Besides  $\text{NaNiPO}_4$ , this sample contains  $\text{Na}_4\text{Ni}_3(\text{PO}_4)_2(\text{P}_2\text{O}_7)$ . According to the two-phase Rietveld refinement, the weight ratio of  $\text{NaNiPO}_4$

and  $\text{Na}_4\text{Ni}_3(\text{PO}_4)_2(\text{P}_2\text{O}_7)$  phases in the sample is 81:19 (Fig. 2). At the Rietveld refinement procedure, the atomic positions in the  $\text{NaMnPO}_4$  structure<sup>22</sup> are taken as a starting model for the refinement of  $\text{NaNiPO}_4$  structural parameters. For the secondary  $\text{Na}_4\text{Ni}_3(\text{PO}_4)_2(\text{P}_2\text{O}_7)$  phase the atomic coordinates from Ref. [23] are taken; these values are fixed during the refinement procedure.



**Fig. 2.** Graphical results of the Rietveld refinement of the  $\text{NaNiPO}_4$  sample showing presence of  $\text{NaNiPO}_4$  (81 wt.%, blue) and  $\text{Na}_4\text{Ni}_3(\text{PO}_4)_2(\text{P}_2\text{O}_7)$  (19 wt.%, red) phases.

Structural parameters of the  $\text{NaNiPO}_4$  compound, obtained for the first time in the present work, are in excellent agreement with the literature data for the isotypical  $\text{NaMPO}_4$  ( $M = \text{Co}, \text{Fe}, \text{Mn}$ ) compounds. In particular, the lattice parameters in the  $\text{NaMPO}_4$  series (Table 2) increases systematically with increasing ionic radii of  $M^{2+}$  ions and the unit cell volumes increase almost linearly in accordance with Vegard's law (Fig. 3) [3]. The values of refined lattice parameters, positional and displacement parameters of atoms in  $\text{NaNiPO}_4$  structure are presented in Table 3. Selected values of bond length and bond angles in the  $\text{NaNiPO}_4$  structure calculated from the refined structural parameters are tabulated in Table 3. According to our knowledge, no lattice parameters or atomic coordinates in the  $\text{NaNiPO}_4$  structure are reported in the literature so far.

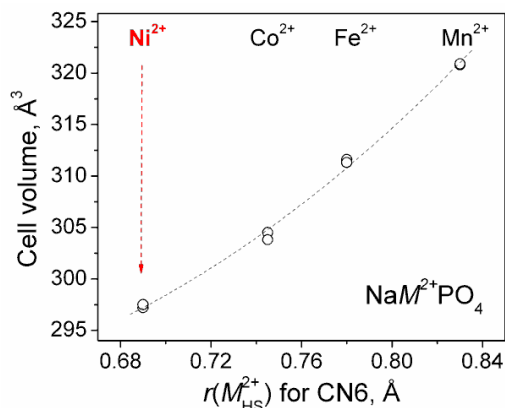


**Fig. 3.** Dependence of the unit cell volumes in  $\text{NaMPO}_4$  ( $M = \text{Ni}, \text{Co}, \text{Fe}, \text{Mn}$ ) series on the ionic radii of  $M^{2+}$  cations.

Similar to the related  $\text{NaMPO}_4$  maricite-type compounds with  $\text{Mn}, \text{Fe}$  and  $\text{Co}$ ,<sup>22,24,25</sup> the  $\text{NaNiPO}_4$  structure can be described as edge-sharing chains of distorted  $\text{NiO}_6$  octahedra running parallel to the  $[100]$ -direction (Fig. 4). Neighbouring chains are cross-connected by almost regular  $\text{PO}_4$  tetrahedra, thus form large

cavities in which the  $\text{Na}$  ions are located. The bond length and bond angles inside  $\text{PO}_4$  tetrahedra in  $\text{NaNiPO}_4$  structure (Table S1) are similar to those in the related  $\text{NaMPO}_4$  compounds,<sup>22,24,25</sup> and the average bond length of 1.537 Å corresponds well to the length of  $\text{P-O}$  bonds in phosphates. The  $\text{NiO}_6$  octahedra are rather distorted, with two compressed and two stretched bonds (Table S1). Besides, distortion of  $\text{NiO}_6$  octahedra is manifested itself in a significant deviation of the intra-octahedral  $\text{O-Ni-O}$  bond angles from  $90^\circ$  (Table S1). Like as in the related  $\text{NaMPO}_4$  compounds, coordination polyhedra of  $\text{Na}$  ions could be also considered as octahedral, however the distortion of  $\text{NaO}_6$  polyhedra is much more pronounced in comparison with  $\text{NiO}_6$  octahedra (Table S1).

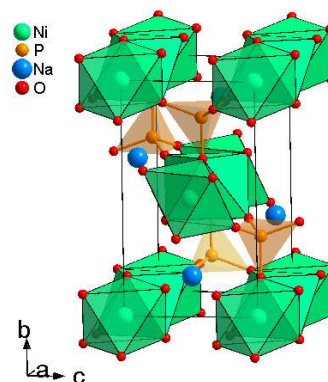


**Fig. 4.**  $\text{NaNiPO}_4$  structure as a frame of the columns of edge-shared  $\text{NiO}_6$  octahedra connected via  $\text{PO}_4$  tetrahedra.

### 3.2 Morphological Analysis

In general, the morphological features are important to mend the electrochemical performance of the material. The formation of porous particles is the characteristic features of combustion method and the amount of pores mainly depend upon the amount of gases released during the reaction. Fig. 5 (a) shows the SEM image of  $\text{NaMnPO}_4$ . It can be seen that the particles are having micro meter in size. The measured sizes of the particles are to be 0.02 to 0.6  $\mu\text{m}$  using scion image software. TEM image (inset of Fig. 5 (a)) of  $\text{NaMnPO}_4$  further supports the formation of larger size particles. Here, the agglomeration of the particles may be due to the high temperature calcination. Similarly, the spherical like particles are observed in  $\text{NaCoPO}_4$  (Fig. 5 (b)) and  $\text{NaNiPO}_4$  (Fig. 5(c)). Subsequently, the presence of porous on the surface of the particles is clearly visible. On the other hand, in  $\text{NaNiPO}_4$ , the presence of smaller sized particles also observed compared to  $\text{NaCoPO}_4$ . Hence, the formation of microsized particles are due to the aggregation of smaller sized particles. So, the presence of pores and smaller sized particles may facilitate to improve the charge storage by the reduction of diffusive path lengths and improves the electrode/electrolyte contact area.<sup>30,31</sup>

### 3.3 Surface Area Analysis

The  $\text{N}_2$  adsorption-desorption isotherms and pore size distribution (BJH-plot) of nanoporous  $\text{NaMPO}_4$  ( $M = \text{Mn}, \text{Co}$  and  $\text{Ni}$ ) particles are shown in Fig. 6. The observed type IV isotherm and BJH-plot for the  $\text{NaNiPO}_4$  and  $\text{NaCoPO}_4$  particles indicates the presence of mesopores on the surface of the particles. For  $\text{NaMnPO}_4$ , Type II isotherm was observed, which confirms the nonporous nature of the particles. Hence, all these well substantiates the FE-SEM result. The calculated specific surface



area ( $S_{\text{BET}}$ ) of  $\text{NaMnPO}_4$ ,  $\text{NaCoPO}_4$  and  $\text{NaNiPO}_4$  porous particles are 17.7, 22.6 and  $18.7 \text{ m}^2 \text{ g}^{-1}$  respectively. The pore size distributions of the samples are calculated by using Barrett-Joyner-Halenda (BJH) method. The obtained average pore diameter of the  $\text{NaCoPO}_4$  ( $\sim 4 \text{ nm}$ ) and  $\text{NaNiPO}_4$  ( $\sim 4 \text{ nm}$ ) particles indicates the presence of mesopores. The high surface area and mesoporous structure of  $\text{NaCoPO}_4$  and  $\text{NaNiPO}_4$  nanoparticles when compared with  $\text{NaMnPO}_4$  will provide more active reaction sites and improve the ions transport.<sup>30</sup>

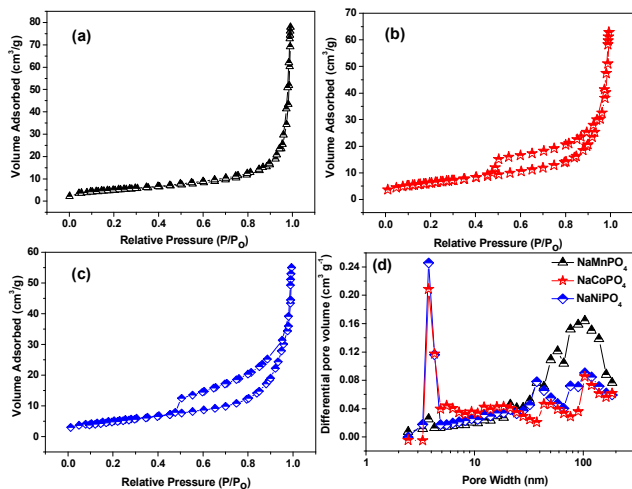
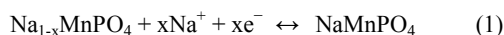


**Fig. 6.** (a)  $\text{N}_2$  adsorption-desorption isotherms of (a)  $\text{NaMnPO}_4$ , (b)  $\text{NaCoPO}_4$  and (c)  $\text{NaNiPO}_4$ . (d) Pore-size distributions of  $\text{NaMPO}_4$

### 3.4 Electrochemical Analysis

In order to well understand the working potential window, redox potential of the active species and charge storage kinetics of the electrode, the cyclic voltammogram analysis was carried in different aqueous electrolytes. CV curves of  $\text{NaMnPO}_4$  in different electrolytes including 1 M  $\text{Na}_2\text{SO}_4$ , 1 M  $\text{NaCl}$ , 1 M  $\text{NaNO}_3$  and 1 M  $\text{NaOH}$  are given in Figure 7. Overall, the potential dependent and independent current regions are observed based on the electrolytes. Specifically, the potential independent current response or rectangular shape CV curves was observed in 1M  $\text{NaCl}$  electrolyte. It infers that the contribution of charge storage was mainly due to the EDLC type *i.e.*, adsorption/desorption of ions at the electrode/electrolyte interfaces. On the other hand, a small redox peak (a potential independent current region) was observed for  $\text{NaMnPO}_4$  at 0.59 V and 0.62V *vs.*  $\text{Ag}/\text{AgCl}$  in 1 M  $\text{Na}_2\text{SO}_4$  and 1 M  $\text{NaNO}_3$  electrolytes, respectively, that revealed the occurrence of intercalation/de-intercalation of  $\text{Na}^+$  ions. Similar type of redox peaks have been reported for  $\text{MnO}_2$ <sup>26a,b</sup>,  $\text{NH}_4\text{MnPO}_4$ <sup>26c</sup> and  $\text{Na}_x\text{MnO}_2$ .<sup>26d</sup> The possible charge storage mechanism of  $\text{NaMnPO}_4$  in 1 M  $\text{Na}_2\text{SO}_4$  and 1 M  $\text{NaNO}_3$  electrolyte is as follows<sup>26</sup>



Where,  $x$  is the mole fraction of inserted sodium ions. The potential difference between the anodic and cathodic peak is smaller than 56 mV, which indicates the good reversibility of the electrode. However the major contribution of the charge storage in neutral aqueous electrolyte depends on adsorption/desorption of  $\text{Na}^+$  ions.

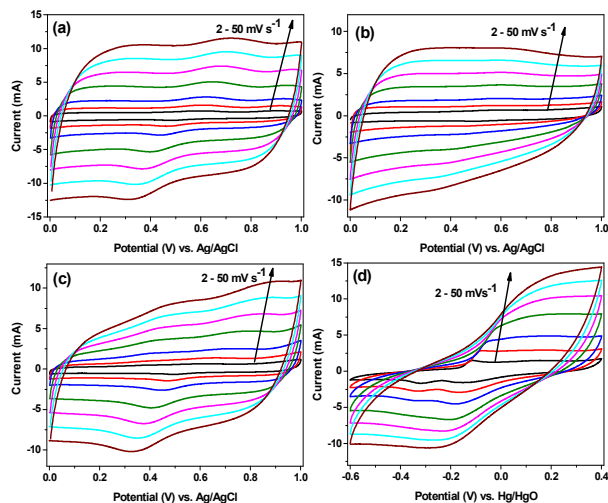


**Fig. 7.** CV curves of  $\text{NaMnPO}_4$  in (a) 1 M  $\text{Na}_2\text{SO}_4$ , (b) 1 M  $\text{NaCl}$ , (c) 1 M  $\text{NaNO}_3$  and (d) 1 M  $\text{NaOH}$  at various scan rates of 2, 5, 10, 20, 30, 40 and  $50 \text{ mV s}^{-1}$ .

Interestingly, a well-defined oxidation/reduction peaks were obtained in 1 M  $\text{NaOH}$  electrolyte (Fig. 7(d)), which indicates the pseudocapacitive behavior of  $\text{NaMnPO}_4$  electrodes. The observed redox peaks in the potential +0.015/-0.281V *vs.*  $\text{Hg}/\text{HgO}$  is due to the Faradic redox reaction of Mn as explained from the Pour-baix diagram.<sup>27</sup> The calculated specific capacitances<sup>30a</sup> are 219, 132, 123 and  $113 \text{ Fg}^{-1}$  for 1 M  $\text{NaOH}$ , 1 M  $\text{NaCl}$ , 1 M  $\text{Na}_2\text{SO}_4$  and 1 M  $\text{NaNO}_3$  respectively, at  $2 \text{ mV s}^{-1}$ . The difference in specific capacitance of  $\text{NaMnPO}_4$  at different electrolytes is due to the difference charge storage mechanism. This may be explained based on the pH and ionic solvation radius of the electrolytes. According to the Pour-baix diagram of Mn, the  $\text{Mn}^{2+}$  ions involve in redox reactions only in alkali aqueous (1 M  $\text{NaOH}$ ) electrolytes and not in neutral aqueous electrolytes like  $\text{NaCl}$ ,  $\text{NaNO}_3$  and  $\text{Na}_2\text{SO}_4$ . The observed redox peaks of  $\text{NaMnPO}_4$  in  $\text{NaOH}$  electrolyte is mainly due to the electron transfer between  $\text{Mn}^{3+}$  and  $\text{Mn}^{2+}$  ions.

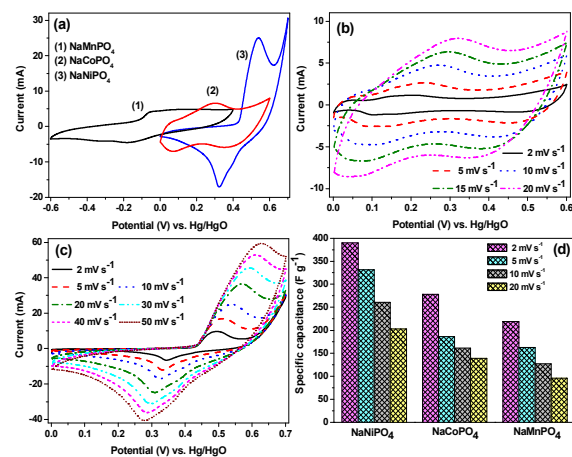


**Fig. 8.** CV curves of (a)  $\text{NaMPO}_4$  at  $10 \text{ mV s}^{-1}$ , (b)  $\text{NaCoPO}_4$  and (c)  $\text{NaNiPO}_4$  in 1 M  $\text{NaOH}$  at different scan rates, (d) SC vs. scan rate for  $\text{NaMPO}_4$  ( $M = \text{Mn, Co and Ni}$ ).

Similarly, the ionic solvation radius of  $\text{OH}^-$  ( $3.00 \text{ \AA}$ ) ions is low compared to  $\text{NO}_3^-$  ( $3.35 \text{ \AA}$ ),  $\text{Cl}^-$  ( $3.32 \text{ \AA}$ ) and  $\text{SO}_4^{2-}$  ( $3.79 \text{ \AA}$ ) ions. Therefore the electrolyte  $\text{OH}^-$  ions can easily diffuse into the pores of the electrode that lodges more number of ions which in

turn high specific capacitance.<sup>28,29</sup> In other words, the ions with smaller ionic solvation radius having high ionic conductivity in aqueous solutions that improves the maximum number of ions to interact with active electrode. Subsequently it creates more active sites in the electrode material.<sup>30b</sup> Overall, low ionic solvation radius of electrolyte anions and pH of the electrolyte has favourably improved the electrochemical performances.

Fig. 8(a) shows the comparative CV curve of NaMPO<sub>4</sub> at 10 mV s<sup>-1</sup> and Fig. 8(b-c) shows the CV curves of NaNiPO<sub>4</sub> and NaCoPO<sub>4</sub> in NaOH electrolyte at various scan rates. Similar to NaMnPO<sub>4</sub>, both the materials also exhibited EDLC and intercalation/de-intercalation behavior in 1 M Na<sub>2</sub>SO<sub>4</sub>, 1 M NaCl, 1 M NaNO<sub>3</sub> and 1M NaOH electrolytes. A couple of redox peaks were observed for both NaNiPO<sub>4</sub> and NaCoPO<sub>4</sub> nanoparticles in 1 M NaOH electrolyte due to intercalation/de-intercalation process, which is clearly seen in Fig. 8(a-c). The redox peak observed in NaNiPO<sub>4</sub> is due to the diffusion controlled reversible redox reaction of Ni(II) ↔ Ni(III).<sup>31-33</sup> The redox reaction of Co(II) ↔ Co(III) is the reason for the peaks obtained at 0.22/0.15 V vs. Hg/HgO in NaCoPO<sub>4</sub>.<sup>31,34</sup> An extra pair of redox peak was observed at 0.55/0.45 V for NaCoPO<sub>4</sub> which is attributed to the redox reaction of Co(III) ↔ Co(IV).<sup>34</sup> The reproducibility of the redox peaks in the CV curves at higher scan rates confirms the good electronic and ionic transport of the material.<sup>31,33</sup> The capacitance value calculated for NaMPO<sub>4</sub>, in various scan rates of 2-20 mV s<sup>-1</sup> is presented in Fig. 8(d). The capacitance value is decreased with increase in scan rate which is due to the decrease in charge diffusion of electrolyte ions into the inner active sites at higher scan rates.<sup>35</sup> It is well agreed with morphological and surface area analysis results. However, the charge storage mechanism is vital role for storing energy.

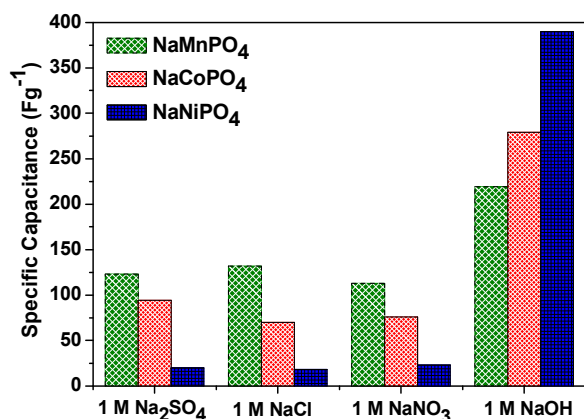


Fig. 9. Capacitance of NaMPO<sub>4</sub> (M = Mn, Co and Ni) in various electrolytes at 2 mV s<sup>-1</sup> scan rate.

For comparison, the calculated voltametric specific capacitance of NaMPO<sub>4</sub> in all Na based aqueous electrolytes is presented in Fig. 9. It can be seen that the NaMPO<sub>4</sub> provides high capacitance in 1 M NaOH electrolyte than other electrolytes, due to its pseudocapacitive behaviour. Hence, it can be optimized that 1 M NaOH is the best electrolyte due to its smaller solvation sphere radius (OH<sup>-</sup>), high ionic conductivity, and better reversibility of the electrode. Particularly, the NaNiPO<sub>4</sub> deliver a high capacitance of 390 F g<sup>-1</sup> at a scan rate of 2 mV s<sup>-1</sup> compared to NaMnPO<sub>4</sub> (219 F g<sup>-1</sup>) and NaCoPO<sub>4</sub> (279 F g<sup>-1</sup>) due to the battery like behaviour and reversible redox reaction of Ni(II) ↔ Ni(III).<sup>31-33</sup> Among the studied sodium metal phosphates, NaNiPO<sub>4</sub> is electrochemically more active than NaMnPO<sub>4</sub> and

NaCoPO<sub>4</sub>. Based on the CV analysis, the combination of NaNiPO<sub>4</sub> and 1 M NaOH are the best electrode and electrolyte. It is well known that the total amount of charge stored in the electrode is mainly due to the contribution of both capacitive and intercalation process.<sup>26</sup> However, the capacitive process consists of two mechanisms including surface redox pseudocapacitive and ions adsorption/desorption reaction at the electrode/electrolyte interface. According to Power's law, the scan rate dependence of CV current can be expressed as<sup>36a-c</sup>

$$i(V) = av^b \quad (2)$$

Where,  $v$  is scan rate (V s<sup>-1</sup>),  $a$  and  $b$  are the adjustable parameters. The slope of  $\log i$  vs  $\log v$  at a fixed potential (V) gives the value of  $b$ . The value of  $b$  has two conditions like  $b=0.5$  for intercalation of ions into the electrode and  $b=1$  for capacitive process. It is the best way to know the charge storage kinetics at each potential. Fig. S3(a) infers that the value of  $b$  is different in different potentials for NaNiPO<sub>4</sub>. It shows that the value of  $b$  is closer to 0.5 at each potential in 1M NaOH electrolyte. Hence, the CV curve is directly proportional to the square root of scan rate. It reveals that the NaNiPO<sub>4</sub> stores the charge based on intercalation/deintercalation mechanism rather than capacitive mechanism (Fig. S3(a)). However, it reveals that the intercalation/deintercalation mechanism is dominant in 1 M NaOH electrolyte for NaNiPO<sub>4</sub>. It is well substantiated the previous result.

The specific capacitance contribution from inner and outer surface of the electrode is calculated using Trasatti plot.<sup>36a-d</sup> The plot between specific capacitance and inverse square root of scan rate implies the specific capacitance contribution from outer surface of the electrode (Fig. S3(b)). Similarly, the plot between specific capacitance vs square root of scan rate implies the specific capacitance contribution from the entire electrode (426 Fg<sup>-1</sup>) (Fig. S3(c)). From this, it can be calculated that the specific capacitance contribution from inner surface of the electrode that is the difference between total surface of the electrode and outer surface of the electrode. Then, the calculated specific capacitance contribution from inner and outer surface of the electrode is 333 and 93 Fg<sup>-1</sup>. It witnessed that the electrode stores more charges in the inner surface of the electrode due to the low ionic solvation radius and high ionic mobility.

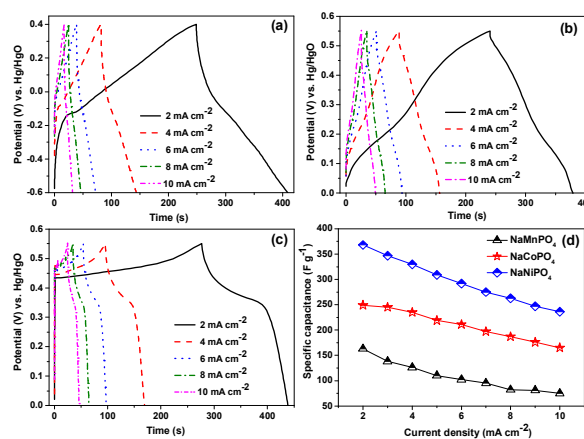


Fig. 10. Galvanostatic charge-discharge curves of (a) NaMnPO<sub>4</sub>, (b) NaCoPO<sub>4</sub> and (c) NaNiPO<sub>4</sub> in 1 M NaOH electrolyte. (d) Specific capacitance vs. current density of NaMPO<sub>4</sub> (M = Mn, Co and Ni).

Hence, galvanostatic charge-discharge measurements were performed in 1 M NaOH for the NaMPO<sub>4</sub> electrodes and are given in Fig. 10. Two different discharge behaviours *i.e.*, linear and non-linear regions are observed for all the cases. The linear region implies that the electrode stores the charge based on adsorption/desorption reaction at the electrode surface. Similarly, the non-linear region is the evidence that the electrode stores the charge based on redox or intercalation mechanism. The asymmetric charge-discharge profiles were obtained for NaMPO<sub>4</sub> (M=Mn, Co and Ni) at all the current densities. It demonstrates the pseudocapacitive nature of the materials. The charge/discharge plateau regions were observed for NaNiPO<sub>4</sub> which demonstrates the battery type charge storage of the material. The plateau regions provide high specific capacitance (above 500 F g<sup>-1</sup>) in narrow potential window and it shows high charge storage capability of the material. The calculated specific capacitance<sup>35</sup> at a current density of 2 mA cm<sup>-2</sup> for NaMnPO<sub>4</sub>, NaCoPO<sub>4</sub> and NaNiPO<sub>4</sub> is 163 F g<sup>-1</sup>, 249 F g<sup>-1</sup> and 368 F g<sup>-1</sup>, respectively. The high capacitance of the NaNiPO<sub>4</sub> compared to other electrodes substantiates the CV results. The specific capacitance of NaMPO<sub>4</sub> as a function of current density is shown in Fig. 10 (d). The specific capacitance was decreased with increase in current density which is normal behaviour. More than 64 % of capacitance at low current density (2 mA cm<sup>-2</sup>) was retained at higher current rates (10 mA cm<sup>-2</sup>) for NaCoPO<sub>4</sub> and NaNiPO<sub>4</sub> which show high rate capability of the materials.

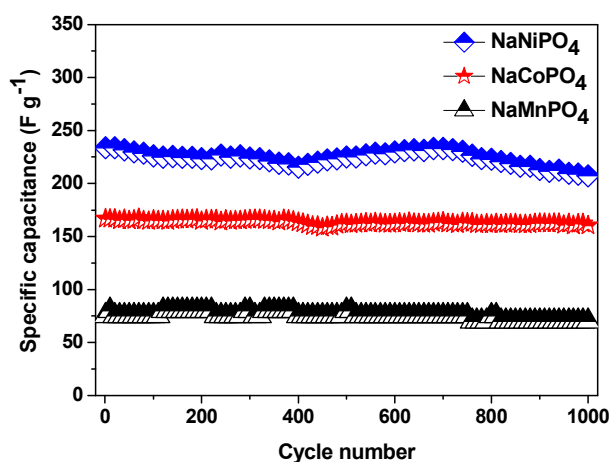


Fig. 11. Variation of the SC with cycle number at 10 mA cm<sup>-2</sup> for NaMPO<sub>4</sub> (M = Mn, Co and Ni).

For practical applications, the cycle life of electrode material is an important parameter. The cycling stability of the materials was tested up to 1000 cycles at a current density of 10 mA cm<sup>-2</sup>. The specific capacitance of NaMPO<sub>4</sub> as a function of cycle number is shown in Fig. 11. No significant capacitance fading was observed for NaMnPO<sub>4</sub> and NaCoPO<sub>4</sub> up to 1000 cycles. 93 and 96 % of initial capacitance was observed for NaMnPO<sub>4</sub> and NaCoPO<sub>4</sub>, respectively. In case of NaNiPO<sub>4</sub> more than 88 % of initial capacitance was retained after 1000 cycles. The results showed good cycling stability of the materials in 1 M NaOH.

### 3.5 Asymmetric AC||NaNiPO<sub>4</sub> supercapacitor characteristics

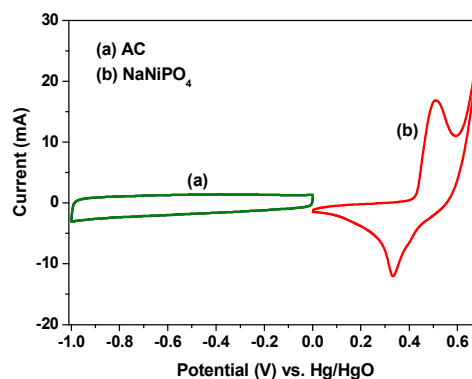


Fig. 12. CV curve of (a) AC and (b) NaNiPO<sub>4</sub> nanoparticles at a scan rate of 5 mV s<sup>-1</sup>.

From the above charge-discharge studies, NaNiPO<sub>4</sub> electrodes delivered more capacitance (368 F g<sup>-1</sup>) compared to NaMnPO<sub>4</sub> and NaCoPO<sub>4</sub>. Therefore an asymmetric full cell (AC||NaNiPO<sub>4</sub>) was fabricated using NaNiPO<sub>4</sub> and activated carbon (AC) as positive and negative electrodes, respectively. The CV curve of NaNiPO<sub>4</sub> and AC in a three electrode system was recorded at a scan rate of 5 mV s<sup>-1</sup> is shown in Fig. 12. The observed rectangular type CV curve of AC confirms the adsorption/desorption of electrolyte cations (Na<sup>+</sup>) and EDLC behavior. The far negative working potential (-1.0 V) of the AC in aqueous electrolyte is promising to use this material as anode material for asymmetric supercapacitors. The specific capacitance calculated from the CV curve is 100 Fg<sup>-1</sup> for AC at a scan rate of 5 mV s<sup>-1</sup>. In the same scan rate, NaNiPO<sub>4</sub> delivered a capacitance of 323 Fg<sup>-1</sup>. It is well known that the positive and negative charge should be balanced (q<sub>+</sub>=q<sub>-</sub>) for fabrication of the full cell.<sup>36c</sup> The mass balancing will follow equation (3),

$$\frac{m_+}{m_-} = \frac{c_-}{c_+} \times \frac{\Delta E_-}{\Delta E_+} \quad (3)$$

Where, m is mass of the active material in the electrode and ΔE is the working potential of the material. On the basis of the specific electric quantity values, the mass for negative electrode is calculated to be ~ 3.9 mg. So the mass loading of the negative electrode material was adjusted to 4 mg. The working potential of the cell is optimized from the CV curve (Fig. 12). The maximum working potential of the asymmetric cell is set to 1.6 V which is higher than that of the AC based symmetric supercapacitor (1.0 V) in alkali aqueous electrolyte.<sup>37-39</sup>

The CV measurements for the asymmetric full cell (AC||NaNiPO<sub>4</sub>) recorded at various scan rates is shown in Fig. 13 (a). The redox peaks observed in the CV curves confirms the pseudocapacitance in positive electrode. An adsorption/desorption of electrolyte cations (Na<sup>+</sup>) at the negative electrode (AC), with the formation of electrical double layer facilitate the charge storage process. The possible electrochemical charge storage reactions in the cell are, for the positive electrode is due diffusion controlled reversible redox reaction of Ni, and for the negative electrode,<sup>40</sup> the mechanism is given below



(here, || indicates double layer)



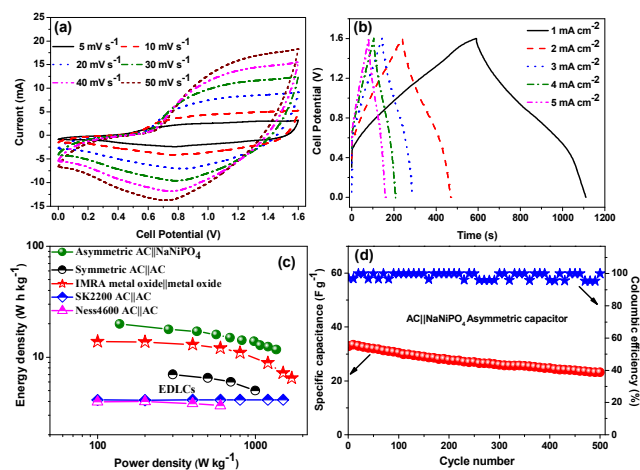


**Fig. 13.** (a) CV and (b) charge-discharge curves for AC||NaNiPO<sub>4</sub> asymmetric supercapacitor, (c) Ragone plot, (d) Cycling stability and coulombic efficiency of AC||NaNiPO<sub>4</sub> asymmetric capacitor at 10 mA cm<sup>-2</sup>.

Galvanostatic charge-discharge curves of the asymmetric capacitor were recorded at various current densities which are shown in Fig. 13 (b). The mirror like form of charge discharge curves shows good electrochemical reversibility of the cell. Subsequently, the non-linear charge-discharge profile is observed which also well substantiates the CV results. The specific capacitance, energy density and power density of the full cell were calculated using the formulae reported elsewhere.<sup>30</sup> The specific capacitance value obtained for the cell from the discharge curves is 56, 50, 41, 36 and 33 F g<sup>-1</sup> at current densities 1, 2, 4, 6, 8 and 10 mA cm<sup>-2</sup>, respectively. Fig. 13 (c) compares the Ragone plots derived from charge/discharge curves at various current densities. The asymmetric capacitor delivers an energy density of 20 Wh kg<sup>-1</sup> at a power density of 138 W kg<sup>-1</sup> and 12 W h kg<sup>-1</sup> even at a high power density of 1358 W kg<sup>-1</sup>. The power and energy density of the asymmetric AC||NaNiPO<sub>4</sub> capacitor is comparatively higher than symmetric (AC||AC) and the current state-of-art electrical double layer capacitor (EDLC) technology.<sup>41</sup> Moreover, the energy density value of the capacitor is significantly higher than the reported AC||NaMnO<sub>2</sub><sup>42</sup> and AC||NaNi<sub>1/3</sub>Co<sub>1/3</sub>Mn<sub>1/3</sub>PO<sub>4</sub><sup>10</sup> hybrid capacitors. However, the energy density is low compared with recent reports of AC||K<sub>0.27</sub>MnO<sub>2</sub>·0.6H<sub>2</sub>O<sup>43</sup> and AC||Na<sub>0.35</sub>MnO<sub>2</sub><sup>44</sup> supercapacitors. The cycle life of the cell was investigated up to 500 cycles. Fig. 13 (d) shows the specific capacitance and coulombic efficiency of the cell tested for 500 charge-discharge cycles at a current density of 10 mA cm<sup>-2</sup>. Superior coulombic efficiency (> 95 %) was observed for the asymmetric cell; capacitance is stable and above 70 % of initial capacitance was retained up to 500 cycles. Overall, the maricite-type NaNiPO<sub>4</sub> is the promising electrode material for energy storage applications based on their good electrochemical reversibility, a high specific capacitance, a smaller particle size, a high surface area, mesoporous structure and a good cycle life.

#### 4. Conclusions

In summary, NaMnPO<sub>4</sub> microstructures and NaMPO<sub>4</sub> (M=Co and Ni) nanoparticles were successfully synthesized by solution combustion synthesis technique. The formation of crystalline NaMPO<sub>4</sub> was identified by XRD Rietveld refinement. Structural parameters of new maricite-type NaNiPO<sub>4</sub> phase were refined.

From N<sub>2</sub> absorption/desorption measurements specific surface area and pore size distributions of the samples were calculated. The electrochemical performance of the materials was first investigated in various Na based aqueous electrolytes and the charge storage mechanism was proposed. The NaNiPO<sub>4</sub> delivered a maximum capacitance of 368 F g<sup>-1</sup> due to intercalation/de-intercalation like behaviour in 1 M NaOH electrolyte, nano meter size of the particles and reversible redox reaction of Ni. An asymmetric full cell (AC||NaNiPO<sub>4</sub>) was fabricated and it delivered a high specific capacitance (56 F g<sup>-1</sup>) and energy density (20 Wh kg<sup>-1</sup>).

#### Notes and references

<sup>a</sup> Solid State Ionics & Energy Devices Laboratory, Department of Physics, Bharathiar University, Coimbatore 641 046, India. Tel: +91-422-2428446; E-mail: selvankram@buc.edu.in

<sup>b</sup> Semiconductor Electronics Department, Lviv Polytechnic National University, 12 Bandera Street, Lviv 79013, Ukraine.

<sup>c</sup> Faculty of Applied Chemical Engineering, Chonnam National University, Gwangju 500-757, Korea

- B. Dunn, H. Kamath and J. M. Tarascon, *Science*, 2011, **334**, 928.
- M. S. Whittingham, *Science*, 1976, **192**, 1126.
- (a) H. Pan, Y-S. Hu and L. Chen, *Energy Environ. Sci.* 2013, **6**, 2338. (b) J. Molenda, A. Kulka, A. Milewska, W. Zajac and K. Swierczek, *Materials*, 2013, **6**, 1656-1987.
- (a) F. Wang, S. Xiao, Y. Hou, C. Hu, L. Liu and Y. Wu, *RSC Adv.*, 2013, **3**, 13059-13084. (b) F. Shi, L. Li, X-L. Wang, C-D. Gu and J-P. Tu, *RSC Adv.*, 2014, **4**, 41910-41921. (c) S. P. Ong, V. L. Chevrier, G. Hautier, A. Jain, C. Moore, S. Kim, X. Ma and G. Ceder, *Energy Environ. Sci.*, 2011, **4**, 3680.
- P. Moreau, B. Guyomard, J. Gaubicher and F. Boucher, *Chem. Mater.*, 2010, **22**, 4126-4128.
- A. D. Tevar and J. F. Waitacre, *J. Electrochem. Soc.*, 2010, **157**, A870-A875.
- J. P. Parant, R. Olazcuaga, M. Devalette, C. Fouassier and P. Hagenmuller, *J. Solid State Chem.*, 1971, **3**, 1-11.
- J. Zhao, J. He, X. Ding, J. Zhou, Y. Ma, S. Wu, R. Huang, *J Power Sources*, 2010, **195**, 6854-6859.
- S. Komaba, C. Takei, T. Nakayama, A. Ogata and N. Yabuuchi, *Electrochem. Commun.*, 2010, **12**, 355-358.
- M. Minakshi, D. Meyrick and D. Appadoo, *Energy and Fuels*, 2013, **27**, 3516-3522.
- D. Kim, E. Lee, M. Slater, W. Lu, S. Rood and C.S. Johnson, *Electrochem. Commun.*, 2012, **18**, 66-69.
- M. Nose, H. Nakayama, K. Nobuhara, H. Yamaguchi, S. Nakanishi and H. Iba, *J Power Sources*, 2013, **234**, 175-179.
- F. Sauvage, L. Laffont, J. M. Tarascon and S. Skaarup, *Inorg. Chem.*, 2007, **46**, 3289-3294.
- D. Yuan, W. He, F. Pei, F. Wu, Y. Wu, J. Qian, Y. Cao, X. Ai and H. Yang, *J. Mater. Chem. A*, 2013, **1**, 3895-3899.
- M. Minakshi and D. Meyrick, *J. Alloys Compd.*, 2013, **555**, 10-15.
- K. T. Lee, T. N. Ramesh, F. Nan, G. Botton and L. F. Nazar, *Chem. Mater.*, 2011, **23**, 3593-3600.
- S-M. Oh, S-T. Myung, J. Hassoun, B. Scrosati and Y-K. Sun, *Electrochem. Commun.*, 2012, **22**, 149-152.
- A. K. Padhi, K. S. Nanjundaswamy and J. B. Goodenough, *J. Electrochem. Soc.*, 1997, **144**, 1188-1194.
- H. Pan, Y-S. Hu and L. Chen, *Energy Environ. Sci.*, 2013, **6**, 2338-2360.
- Y. Zhu, Y. Xu, C. Luo and C. Wang, *Nanoscale*, 2013, **5**, 780-787.
- K. Zhagib, J. Trottier, P. Hovington, F. Brochu, A. Guerfi, A. Mauger and C. M. Julien, *J Power Sources*, 2011, **196**, 9612-9617.
- J. Moring, E. Kostiner, *J. Solid State Chem.*, 1986, **61**, 379-383.
- P.G. Nagorny, A.A. Kapshuk, A.N. Sobolev, N.V. Golego, *Kristallografiya*, 1996, **41**, 835-838.
- J.N. Bridson, S.E. Quinlan, and P.R. Tremaine, *Chem. Mater.* 1998, **10**, 763-768
- R. Hammond, J. Barbier, *Acta Cryst.*, 1996, **B52**, 440-449.

26. (a) S. Pang, A. M. Anderson, *J. Mater. Chem.*, 2000, **15**, 2096-2106. (b) Y-H. Chu, C-C. Hu, K-H. Chang, *Electrochim. Acta*, 2012, **61**, 124-131. (c) H. Pang, Z. Yan, W. Wang, Y. Wei, X. Li, J. Li, J. Chen, J. Zhang and H. Zheng, *Int. J. Electrochem. Sci.*, 2012, **7**, 12340-12353. (d) L. Mai, H. Li, Y. Zhao, L. Xu, X. Xu, Y. Luo, Z. Zhang, W. Ke, C. Niu and Q. Zhang, *Scientific Reports*, 2013, **3**, 1718, 1-6.
27. M. Pourbaix, Atlas of Electrochemical Equilibria in Aqueous Solutions, Pergamon, New York, 1966.
28. C-C. Hu and C-C. Wang, *J. Power Sources*, 2004, **125**, 299-308.
29. F. Cheng, C. He, D. Shi, H. Chen, J. Zhang, S. Tang, D. E. Finlow, *Mater. Chem. Phys.*, 2011, **131**, 268-273.
30. (a) B. Senthilkumar, M. Danielle, Y-S. Lee and R. Kalai Selvan, *RSC Adv.*, 2013, **3**, 16542-16548. (b) K. V. Sankar, D. Kalpana, R. K. Selvan, *J. Appl. Electrochem.*, 2012, **42**, 463-470.
31. (a) B. Senthilkumar, K. Vijaya Sankar, R. Kalai Selvan, M. Danielle and M. Manickam, *RSC Adv.*, 2013, **3**, 352-357.
32. C. C. Hu, J. C. Chen and K. H. Chang, *J. Power Sources*, 2013, **221**, 128-133.
33. G. Wang, L. Zhang, J. Kim and J. Zhang, *J. Power sources*, 2012, **217**, 554-561.
34. M-C. Liu, L-B. Kong, X-J. Ma, C. Lu, X-M. Li, Y-C. LuO and L. Kang, *New. J. Chem.*, 2012, **36**, 1713-1716.
35. M. Aghazadeh, A. N. Golikand and M. Ghaemi, *Int. J. Hydrogen Energy*, 2011, **36**, 8674-8679.
36. (a) M. Sathiya, A. S. Prakash, K. Ramesha, J.M. Tarascon, A. K. Shukla, *J. Am. Chem. Soc.* 2011, **133**, 16291-16299. (b) Jonathon Duay, Stefanie A. Sherrill, Zhe Gui, Eleanor Gillette, and Sang Bok Lee, *ACS Nano* 2013, **7**, 1200-1214. (c) Haihong Yina, Changqing Song, Yang Wang, Shouchuan Li, Min Zeng, Zhengli Zhang, Ziqiang Zhu, Ke Yu, *Electrochim. Acta* 2013, **111**, 762-770, (d). K. V. Sankar, R. K. Selvan, *RSC Advances* 2014, **4**, 17555-17566, (e). J. Cao, Y. Wang, Y. Zhou, J-H. Ouyang, D. Jia and L. Guo, *J. Electroanal. Chem.*, 2013, **689**, 201-206.
37. E. G. Calvo, F. Lufitano, P. Staiti, A. Brigandi, A. Arenillas and J. A. Menendez, *J. Power Sources*, 2013, **241**, 776-782.
38. X. Sun, X. Zhang, H. Zhang, D. Zhang and Y. Ma, *J. Solid State Electrochem.*, 2012, **16**, 2597-2603.
39. L-B. Kong, M. Lu, J-W. Lang, Y-C. Luo and L. Kang, *J. Electrochem. Soc.*, 2009, **156**, A1000-A1004.
40. Y. Zhao, Q. Y. Lai, Y. J. Hao, and X. Y. Ji, *J. Alloys Compd.*, 2009, **471**, 466-469.
41. Burke, A. F. Proc. IEEE Veh. Power Propulsion Conf. (VPPC'05), 2005, 356-366.
42. Q. T. Qu, Y. Shi, S. Tian, Y. H. Chen, Y. P. Wu and R. Holze, *J. Power Sources*, 2009, **194**, 1222-1225.
43. Q. Qu, L. Li, S. Tian, W. Guo, Y. P. Wu and R. Holze, *J. Power Sources*, 2009, **195**, 2789-2794.
44. B. H. Zhang, Y. Liu, Z. Chang, Y. Q. Yang, Z. B. Wen, Y. P. Wu and R. Holze, *J. Power Sources*, 2014, **253**, 98-103.

**Table 1.** Lattice parameters of the NaMPO<sub>4</sub> (M=Mn and Co) phases in comparison with the literature data

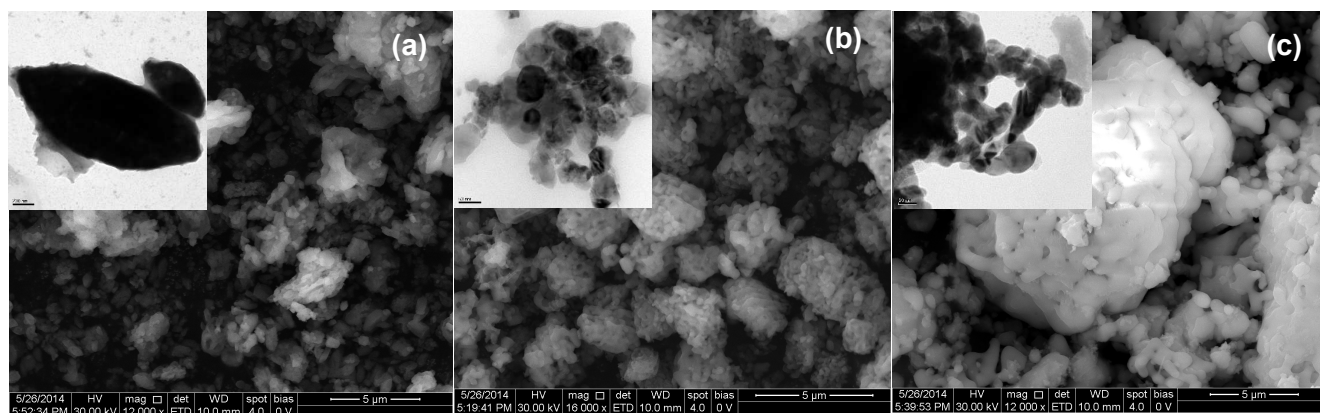
Composition	Space group	a, Å	b, Å	c, Å	V, Å <sup>3</sup>	Reference
NaMnPO <sub>4</sub>	<i>Pmnb</i>	6.9053(9)	9.085(2)	5.1149(7)	320.9(2)	This work
NaMnPO <sub>4</sub>	<i>Pmnb</i>	6.9041(1)	9.0882(1)	5.1134(1)	320.8	[22]
NaCoPO <sub>4</sub>	<i>P6<sub>5</sub></i>	10.169(3)	-	23.868(7)	2137.5(9)	This work
<i>h</i> -NaCoPO <sub>4</sub>	<i>P6<sub>5</sub></i>	10.166(1)	-	23.881(5)		JCPDS no. 52-335

**Table 2.** Lattice parameters of NaNiPO<sub>4</sub> sample in comparison with the literature data for the related maricite-type NaMPO<sub>4</sub> (M=Co, Fe, Mn) compounds.

Composition	Space Group	a, Å	b, Å	c, Å	V, Å <sup>3</sup>	Reference
NaNiPO <sub>4</sub>	<i>Pmnb</i>	6.7373(7)	8.7735(10)	5.0336(6)	297.5(1)	This work
NaCoPO <sub>4</sub>	<i>Pnma</i>	8.871(3)	6.780(3)	5.023(1)	302.1	JCPDS no. 87-1016
	<i>Pnma</i>	8.896(1)	6.8007(9)	5.0341(7)	304.5	JCPDS no. 88-481
NaFePO <sub>4</sub>	<i>Pmnb</i>	6.867	8.989	5.049	311.6	JCPDS no. 29-1216
	<i>Pnma</i>	8.990	6.862	5.047	311.3	JCPDS no. 89-816
NaMnPO <sub>4</sub>	<i>Pmnb</i>	6.9041(1)	9.0882(1)	5.1134(1)	320.8	JCPDS no.84-852

**Table 3.** Crystallographic data for  $\text{NaNiPO}_4$  structure (space group  $Pmbn$ ,  $Z = 4$ ,  $a = 6.7373(7) \text{ \AA}$ ,  $b = 8.7735(10) \text{ \AA}$ ,  $c = 5.0336(6) \text{ \AA}$ )

Atoms, sites	$x/a$	$y/b$	$z/c$	$B_{\text{iso/eq}}, \text{ \AA}^2$
Na, 4c	$\frac{3}{4}$	0.8544(15)	0.553(2)	1.5(3)
Ni, 4a	0	0	0	1.1(2)
P, 4c	$\frac{1}{4}$	0.8206(11)	0.535(2)	1.1(3)
O1, 4c	$\frac{1}{4}$	0.882(2)	0.243(2)	0.5(4)
O2, 8d	0.4365(14)	0.8756(15)	0.6732(15)	0.7(4)
O3, 4c	$\frac{1}{4}$	0.6442(14)	0.539(3)	0.3(5)

**Fig. 5.** FE-SEM images of nanoporous (a)  $\text{NaMnPO}_4$ , (b)  $\text{NaCoPO}_4$  and (c)  $\text{NaNiPO}_4$  particles (inset) TEM image.